



**CHALMERS**  
UNIVERSITY OF TECHNOLOGY

## **Beyond breakaway corrosion – Influence of chromium, nickel and aluminum on corrosion of iron-based alloys at 600 °C**

Downloaded from: <https://research.chalmers.se>, 2024-04-19 22:03 UTC

Citation for the original published paper (version of record):

Persdotter, A., Eklund, J., Liske, J. et al (2020). Beyond breakaway corrosion – Influence of chromium, nickel and aluminum on corrosion of iron-based alloys at 600 °C. Corrosion Science, 177. <http://dx.doi.org/10.1016/j.corsci.2020.108961>

N.B. When citing this work, cite the original published paper.



# Beyond breakaway corrosion – Influence of chromium, nickel and aluminum on corrosion of iron-based alloys at 600 °C

A. Persdotter, J. Eklund, J. Liske, T. Jonsson

Division of Energy and Materials, Chalmers University of Technology, SE-412 96, Sweden

## ARTICLE INFO

### Keywords:

High temperature corrosion  
Breakaway oxidation  
Model alloys  
Iron oxide  
Oxide microstructure  
Primary and Secondary corrosion protection

## ABSTRACT

Breakaway corrosion remains a challenge for many high temperature applications. The oxide formed after breakaway is commonly considered non-protective. This study investigates the protective properties after breakaway on a wide set of (Fe,Cr,Al/Ni)-model alloys by thermogravimetric analysis, ion/electron microscopy and X-ray spectroscopy. The results show that the oxide scales formed after breakaway exhibit similar microstructural features on all FeCr(Ni/Al)-alloys, and that the growth rate is greatly influenced by alloy composition for some alloys while it has little influence on others. This observation may be of great help in the selection and development of materials for use in harshly corrosive environments.

## 1. Introduction

High temperature corrosion of Fe-based alloys remains a challenge in many high temperature applications. To overcome this challenge alloying elements such as Cr and Al are often added to provide an improved corrosion protection at intermediate to high temperatures (~400–1200 °C). There is a great number of publications concerning the oxidation properties of Fe-based alloys, summarized, e.g. by Kofstad [1], Birks and Meier [2] and Young [3]. The corrosion protection of stainless steels and FeCrAl alloys exposed in mild environments rely on the formation of a slow-growing Cr-rich (stainless steels) or Al/Cr-rich (FeCrAl alloys)  $M_2O_3$  oxide scale. These oxide scales are the designed corrosion resistance of stainless steels and FeCrAl alloys and is here referred to as their primary corrosion protection. Typical for the primary corrosion protection is that the oxide growth rate is slow and limited by ion diffusion. Thus, the oxide growth of the primary corrosion protection is possible to model by diffusion-based modeling tools such as, e.g. DICTRA [4]. Low alloyed steels do not have sufficient amounts of Cr to form a primary corrosion protection. Thus, low alloyed steels only have one type of corrosion protection, composed of a multi-layered Fe-rich oxide scale.

In more corrosive environments, the primary corrosion protection tend to break down (breakaway corrosion) and the progress of the corrosion attack is mechanistically changed. The oxide scales formed after breakaway are faster-growing Fe-rich oxides, with similar features to those formed on low alloyed steels. The mechanisms behind breakaway corrosion of stainless steels and FeCrAl alloys has been thoroughly

investigated in many previous studies [5–27] and are reviewed by, e.g. Saunders et al. [28] and Fry et al. [29]). The breakdown of the primary corrosion protection is a major issue for many applications where corrosion limits the lifetime of key components, in, e.g. biomass- and waste-fired boilers [30–35]. Thus, the main research focus of many previous studies have been put on how to improve the primary corrosion protection and prevent or delay the breakdown of this oxide scale.

The breakdown and transition from a thin protective Cr/Al-rich oxide to a thicker, fast-growing Fe-rich oxide is commonly referred to as breakaway corrosion, indicating that the corrosion protection has been lost. However, recent studies indicates that the oxide scale formed after breakaway at intermediately high temperatures (e.g. 600 °C) may act partly protective and that its protective properties can be improved (see, e.g. [9,36]). Thus, the protection of the oxide scale formed after breakaway may be referred to as the secondary corrosion protection. The oxide scales formed after breakdown of the primary corrosion protection, i.e. in the secondary corrosion regime, have been shown to be multi-layered and composed of an outward-growing Fe oxide ( $Fe_2O_3/Fe_3O_4$ ) and an inward-growing mixed spinel ( $(Fe,Cr,M)_3O_4$ ). Pujilaksono et al. [20], Jonsson et al. [25,27,37] and Gheno et al. [21, 38] studied the oxides formed on Fe-based alloys after breakaway at 600–650 °C in several different environments ( $O_2 + H_2O$ ,  $O_2 + K_2CO_3$ ,  $O_2 + H_2O + KCl$ ,  $O_2 + H_2O + SO_2 + KCl$ ,  $H_2 + H_2O + Ar$ ,  $O_2 + K_2CO_3$ ,  $Ar + CO_2$ ,  $Ar + H_2O + CO_2$ ). Despite the different environments and exposure conditions the studies showed that the same type of multi-layered Fe-rich oxide scale formed after breakaway. Since the primary corrosion protection rapidly breaks down, the lifetime of many

E-mail address: [amanda.persdotter@chalmers.se](mailto:amanda.persdotter@chalmers.se) (A. Persdotter).

<https://doi.org/10.1016/j.corsci.2020.108961>

Received 9 March 2020; Received in revised form 14 August 2020; Accepted 17 August 2020

Available online 20 August 2020

0010-938X/© 2020 The Authors. Published by Elsevier Ltd. This is an open access article under the CC BY license (<http://creativecommons.org/licenses/by/4.0/>).

alloys exposed in harshly corrosive environment must rely on the scales formed after breakaway corrosion. Thus, the concept of secondary corrosion protection of alloys is introduced to increase the awareness of the possibilities to improve the protective properties of the oxide scale formed after breakaway. While the primary corrosion protection has been investigated to a large extent, systematic studies on the protective properties of the oxide scale formed in the secondary corrosion regime are scarce.

This study investigates how the protective properties of the scale formed on Fe-based alloys after breakaway (at 600 °C) may change as the alloy composition is altered. This is done by well-controlled exposures of a wide set of Fe-based model alloys with varying amounts of Cr, Ni and Al. In order to investigate the secondary corrosion regime, the break-down of the primary corrosion protection ((Cr,Al)<sub>2</sub>O<sub>3</sub>) is triggered by adding K<sub>2</sub>CO<sub>3</sub>(s). The oxidation kinetics is studied by thermogravimetric analysis (TGA) and linked to the oxide scale microstructure in order to make a thorough comparison between different alloy compositions. The study elucidates the importance of separating different corrosion regimes from a modeling perspective by defining the concept of primary and secondary corrosion regimes for the oxide scales formed before and after breakaway. The terminology and results from this study are valuable for developers of modeling tools such as, e.g. DICTRA [4, 39], to simplify the systems for future lifetime predictive models, as well as for material developers and for selection of materials for use in high temperature applications where breakaway corrosion cannot be prevented.

## 2. Experimental procedure

The influence of alloying elements was studied on FeCr, FeCrNi and FeCrAl model alloys exposed in 5% O<sub>2</sub> + 95% N<sub>2</sub> at 600 °C in the presence and absence of K<sub>2</sub>CO<sub>3</sub>. The formed oxide scales were analyzed and characterized by ion and electron microscopy and spectroscopy. The samples exposed to K<sub>2</sub>CO<sub>3</sub> were analyzed in cross section in order to better characterize the microstructure.

### 2.1. Sample preparation

The model alloys were delivered by Kanthal and produced by induction heating and cast in a copper mold under an argon atmosphere. Prior to hot rolling the cylindrical ingots were machined to remove surface defects and heated at 1150 °C to a strip sample (13 × 3 mm). The samples were reheated approximately four times during the hot rolling process, and heat treated after hot rolling, in order to achieve a suitable grain size. The heat treatments were done at 950 °C (1 h) for the ferritic alloys and 1050 °C (30 min) for the austenitic alloys. The complete material-matrix is summarized in Table 1 including composition, measured alloy grain size as well as expected crystal structure (calculated for equilibrium at 600 °C with Thermocalc software). The alloy grain sizes were investigated by light optical microscopy (LOM) on chemically etched samples. The chemical etching was performed in different solutions depending on the alloy. For the FeCrAl model alloys (and FeCr) the etching was performed at 60 °C in a solution of HCl/H<sub>2</sub>O (50:50), while the etching of the FeCrNi model alloys was performed in HCl/HNO<sub>3</sub>/H<sub>2</sub>O (45:45:10) above 60 °C.

The received model alloys were cut into coupons with sample dimensions 11 × 11 × 2 mm for tube furnace exposures and 8 × 10 × 2 mm for thermogravimetric analysis (TGA). Prior to exposure the samples were ground on SiC paper (P4000) and subsequently polished with 3 and 1 μm diamond suspension to mirror-like appearance. The samples were degreased in acetone using ultrasonic agitation.

To study the secondary corrosion regime (oxide formed after breakaway), potassium carbonate (1 mg/cm<sup>2</sup> K<sub>2</sub>CO<sub>3</sub>) was deposited onto the polished samples prior to exposure. The K<sub>2</sub>CO<sub>3</sub> has previously been shown to induce breakaway corrosion by Cr-depletion of the Cr-rich oxide scales (i.e. breakdown of the primary protection) [19,24]

**Table 1**

Nominal composition, grain size and calculated crystal structure at equilibrium (600 °C) for the investigated model alloys. \* Calculated by H. Larsson, KTH, at 600 °C (exposure temperature) at equilibrium using Thermocalc software (TC).

Alloy	Cr	Ni	Al	Fe	Grain size (alloy) [μm]	Crystal structure*
<i>FeCr alloys</i>						
Fe2.25Cr	2.25	–	–	98	–	Ferrite (BCC)
Fe10Cr	10	–	–	90	–	Ferrite (BCC)
Fe18Cr	18	–	–	82	150	Ferrite (BCC)
Fe25Cr	25	–	–	75	–	Ferrite (BCC)
<i>FeCrNi alloys</i>						
Fe18Cr	18	0	–	82	150	Ferrite (BCC)
Fe18Cr2Ni	18	2	–	80	90	Ferrite (BCC)
Fe18Cr5Ni	18	5	–	77	8	90:10 (BCC/ FCC)
Fe18Cr10Ni	18	10	–	72	60	50:50 (BCC/ FCC)
Fe18Cr20Ni	18	20	–	62	60	Austenite (FCC)
Fe18Cr34Ni	18	34	–	48	70	Austenite (FCC)
<i>FeCrAl alloys</i>						
Fe5Cr3Al	5	–	3	92	500	Ferrite (BCC)
Fe10Cr3Al	10	–	3	87	650	Ferrite (BCC)
Fe18Cr3Al	18	–	3	79	400	Ferrite (BCC)
Fe18Cr1Al	18	–	1	81	280	Ferrite (BCC)
Fe18Cr6Al	18	–	6	76	200	Ferrite (BCC)
Fe25Cr3Al	25	–	3	72	350	Ferrite (BCC)

and allows for analysis of the secondary corrosion regime without the influence of other corrosive species such as Cl. The K<sub>2</sub>CO<sub>3</sub> was deposited by spraying a saturated solution of salt in water. Gravimetric measurements were made using a Sartorius balance with microgram resolution. The samples were subsequently dried in air and stored in a desiccator (drying agent P<sub>2</sub>O<sub>5</sub>) prior to exposure and awaiting analysis post exposure to avoid atmospheric corrosion.

Wide cross sections of a selection of the exposed samples were prepared by broad ion beam (BIB) milling in order to study the microstructure of the oxide scales formed in the secondary corrosion regime. The BIB used in this study was a Leica EM TIC 3X BIB equipped with a triple Ar ion gun operated at 8 kV. Some of the samples were additionally milled at 4 kV in order to improve the surface for SEM-imaging at low keV. Prior to milling the steel coupons were sputtered with gold, covered by a Si wafer and subsequently cut, without lubrication, by a low speed saw.

### 2.2. Exposures

The corrosion protection and influence of composition was investigated by furnace exposures at 600 °C with varying amounts of Ni, Cr and Al. A minimum of three samples of each model alloy were exposed. All alloys were exposed in 5% O<sub>2</sub> + 95% N<sub>2</sub> with and without 1 mg/cm<sup>2</sup> K<sub>2</sub>CO<sub>3</sub>. All model alloys used for studying the primary protection (without K<sub>2</sub>CO<sub>3</sub>) were exposed in a horizontal tube furnace (flowrate: 3 cm/s) for 24 h. The samples used for studying the secondary protection (with K<sub>2</sub>CO<sub>3</sub>) were exposed in a Setaram Setsys thermobalance (flowrate: 1.5 cm/s) to record the oxidation kinetics by thermogravimetric analysis (TGA). The samples were positioned parallel to the direction of the gas flow in both furnace setups.

In order to better link the mass gain study and the microstructural investigation the oxide scale thicknesses, *x*, were estimated from mass gain data (*W* [g/cm<sup>2</sup>]) for each alloy (see Eq. (1)):

$$x = \frac{W}{\rho \frac{aM_O}{aM_O + bM_M}} \quad (1)$$

The calculations were performed assuming the oxide scales to be dense, with density  $\rho$ , and composed of one predefined oxide ( $M_aO_b$ : Fe<sub>3</sub>O<sub>4</sub> for Fe-rich oxides and Cr<sub>2</sub>O<sub>3</sub> for the Cr/Al-rich oxides). The density is corrected for with the factor  $\frac{aM_O}{aM_O + bM_M}$ , to include only the mass gain resulting

from oxygen uptake from the atmosphere.

### 2.3. Analytical techniques

The oxide scales were imaged and analyzed by a combination of ion and electron microscopy as well as Energy dispersive X-ray spectroscopy (EDX). The electron microscopy was performed on an FEI Quanta ESEM 200 and a Zeiss LEO Ultra 55 FEG SEM, both equipped with a field emission gun and an EDX detector for chemical analysis. The microscopes were operated in high vacuum mode with an accelerating voltage of 10–20 keV for BSE imaging and chemical analysis as well as 1.5–2.5 keV for higher resolution in the LEO Ultra. Both secondary electrons (SEs) and backscattered electrons (BSEs) were used for imaging, but mainly BSEs are shown in this paper.

The focused ion beam (FIB) was primarily used to image the oxide grains, since the channeling contrast is enhanced with ion microscopy. The instrument used was an FEI Versa3D LoVac DualBeam, equipped with a Ga liquid metal ion source (LMIS) and operated in high vacuum mode at an acceleration voltage of 30 kV and a beam current of 10 pA. In order to obtain better grain-contrast the cross sections were imaged several times in a row using ion induced secondary electrons (ISEs). The grain sizes were measured perpendicular to the growth direction of the oxide scale, assuming these grain boundaries to be the most relevant pathways for ion diffusion.

### 3. Results

The influence of alloy composition was investigated regarding oxide growth rate in mild environments (primary corrosion regime) and oxide growth rate/microstructure after breakaway corrosion (secondary corrosion regime). Three different sets of model alloys were investigated:

- FeCr (influence of Cr)
- FeCrNi (influence of Ni)
- FeCrAl (influence of Al and Cr)

The model alloys were exposed at 600 °C for 24 hrs in two environments and the results are divided accordingly:

- Mild environment (5% O<sub>2</sub> + 95% N<sub>2</sub>) – primary corrosion regime.
- Harsh environment (5% O<sub>2</sub> + 95% N<sub>2</sub> + K<sub>2</sub>CO<sub>3</sub>(s)) – secondary corrosion regime.

#### 3.1. Oxidation kinetics

The concept of primary and secondary corrosion regimes, introduced in this study, is illustrated by growth kinetics in Fig. 1. The primary corrosion protection (see A<sub>1</sub>) is a slow-growing oxide which may break down, in the presence of, e.g. K<sub>2</sub>CO<sub>3</sub>, to form a faster growing Fe-rich oxide scale (secondary corrosion regime, see A<sub>2</sub>). The results from this study showed that the incubation time to breakaway may vary (see curve A, B) as well as the growth rate of the oxide scales formed in the primary (see A<sub>1</sub>, D) and secondary corrosion regimes (see A<sub>2</sub>, B, C) as illustrated in Fig. 1.

##### 3.1.1. General observations

Fig. 3 shows the gravimetric results for FeCr, FeCrNi and FeCrAl model alloys exposed for 24 h at 600 °C in 5% O<sub>2</sub> + 95% N<sub>2</sub> in the presence and absence of K<sub>2</sub>CO<sub>3</sub>(s). Most alloys exposed in the mild environment (primary corrosion protection) showed mass gains indicating very thin oxide scales ( $W_{1st} < 0.35 \text{ mg/cm}^2$ , most  $< 0.02 \text{ mg/cm}^2$ ) while all alloys, except for Fe18Cr6Al, exposed in K<sub>2</sub>CO<sub>3</sub> showed high mass gains ( $W_{2nd} \approx 10\text{--}500 \times W_{1st}$ ). Thus, the results clearly

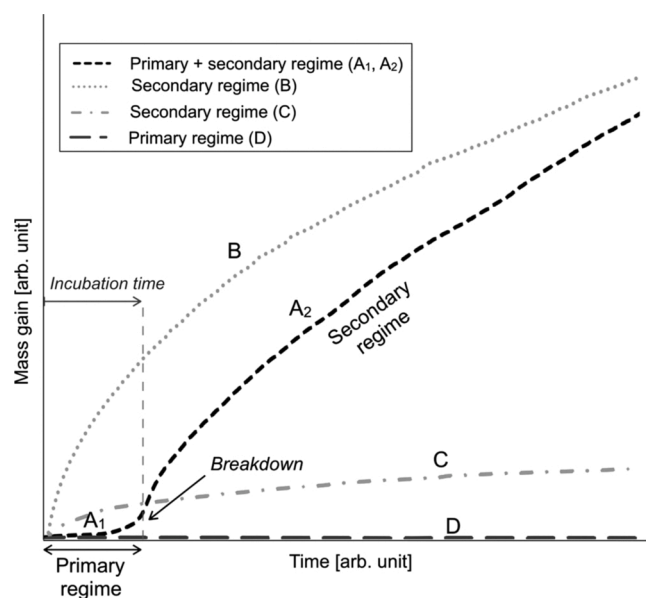


Fig. 1. Kinetic illustration of the primary (A<sub>1</sub>, D) and secondary (A<sub>2</sub>, B, C) corrosion protection of Fe-based alloys. The primary (A<sub>1</sub>) and secondary (A<sub>2</sub>) regimes are marked in the figure along with the breakaway event and incubation time. Note that the breakaway event occurs instantly in curve B and C.

illustrate the two corrosion regimes before (primary regime) and after (secondary regime) breakaway corrosion.

The primary corrosion regime was studied mainly as a reference to better understand the secondary corrosion regime. Note that the exposures without K<sub>2</sub>CO<sub>3</sub> (primary corrosion regime) were performed in a tube furnace while the K<sub>2</sub>CO<sub>3</sub> exposures (secondary corrosion regime) were performed by TGA in order to rule out different incubation times to breakaway corrosion, i.e. different propagation times in the secondary regime. Mass gains are expected to be comparable for the two exposure techniques, concluded after exposing several samples in both the tube furnace and by TGA. The data represents the end points, which is why the incubation time to breakaway is important to study the secondary corrosion regime. The incubation times are summarized in Table 2. Most alloys exhibited very short (<1 h) incubation times to breakaway in the presence of K<sub>2</sub>CO<sub>3</sub>. The exceptions were the Fe18Cr and Fe18Cr2Ni alloys (<6 hrs) and the Fe18Cr5Ni which showed an incubation time of approximately 20 hrs. Thus, the mass gains after 24 hrs exposure are considered good representations of the growth rate also in the secondary corrosion regime, with caution taking to the absolute mass gain value of the Fe18Cr5Ni alloy.

##### 3.1.2. Corrosion in mild environments – primary corrosion regime

The mass gain data, and corresponding estimated thicknesses, for the primary corrosion protection (see Fig. 2) indicated that the majority of the alloys formed thin oxide scales under the present exposure conditions. The exceptions were the alloys with higher Ni-content (Fe18Cr34Ni), as well as the alloy with 5 wt% Cr (Fe5Cr3Al). Data was used as comparison from Pujilaksono et al. [20] for the binary FeCr alloys ( $x = 2.25, 10, 18, 25 \text{ wt\% Cr}$ ) exposed under the same exposure conditions (600 °C, 5% O<sub>2</sub> + 95% N<sub>2</sub>) for 24 hrs showing high mass gain for the alloy with low Cr content (Fe2.25Cr) and low mass gains for the other alloys (see Fig. 2). The mass gain data were recalculated to oxide scale thicknesses for all alloys, assuming the formation of a dense Cr<sub>2</sub>O<sub>3</sub> for the alloys exhibiting low mass gains and a dense Fe<sub>3</sub>O<sub>4</sub> for the 5 wt% Cr (Fe5Cr3Al) and the 34 wt% Ni (Fe18Cr34Ni) alloys. The choice of oxide for the calculations were based on the mass gain data, plan view SEM/EDX characterization and a literature review. The calculated oxide scale thicknesses were in the range of 45–105 nm for the Cr/Al-rich oxide scales (Fe18Cr, Fe10Cr3Al, Fe18Cr3Al, Fe25Cr3Al, Fe18Cr1Al,

**Table 2**

Approximate incubation times to breakaway for the FeCr, FeCrNi, and FeCrAl model alloys exposed for 48 h (TGA; 5% O<sub>2</sub> + 95% N<sub>2</sub> at 600 °C) in the presence of K<sub>2</sub>CO<sub>3</sub>. Most of the alloys exhibit very short incubation times, with the exceptions being the Fe18Cr, Fe18Cr2Ni and Fe18Cr5Ni. The oxidation kinetics on a few alloys indicate no breakaway event. Thus no incubation times are reported for these alloys.

Alloy	Incubation time [h]
<i>FeCr alloys</i>	
Fe2.25Cr	<1
Fe10Cr	<1
Fe18Cr	<1
Fe25Cr	–
<i>FeCrNi alloys</i>	
Fe18Cr	<6
Fe18Cr2Ni	<6
Fe18Cr5Ni	~20
Fe18Cr10Ni	<1
Fe18Cr20Ni	<1
Fe18Cr34Ni	<1
<i>FeCrAl alloys</i>	
Fe5Cr3Al	<1
Fe10Cr3Al	<1
Fe18Cr3Al	<1
Fe18Cr1Al	<1
Fe18Cr6Al	–
Fe25Cr3Al	<1

Fe18Cr6Al, Fe18Cr2Ni, Fe18Cr5Ni, Fe18Cr10Ni) and 1.8–2.5 µm for the Fe-rich oxide scales (Fe5Cr3Al, Fe18Cr34Ni). The Fe18Cr20Ni alloy formed Fe-rich oxide on parts of the sample surface. Thus, the calculated thickness (~130 nm) is not a good estimation of the actual thickness of the primary corrosion protection of this alloy.

### 3.1.3. Corrosion in harsh environments – secondary corrosion regime

The mass gain data (see Fig. 3) and the oxidation kinetics showed that the primary corrosion protection of all alloys, except for Fe18Cr6Al and Fe25Cr, broke down in the presence of K<sub>2</sub>CO<sub>3</sub>. Growth kinetics and mass gains were orders of magnitude higher than the corresponding primary corrosion protection. Thus, it could be concluded that all alloys, except for Fe18Cr6Al and Fe25Cr, had entered the secondary corrosion regime. The estimated thicknesses based on the mass gain data of the secondary corrosion regime ranged from 0.8 to 32 µm after 24 hrs exposure and from 1 to 54 µm after 48 h exposure. This is to be compared with the estimated thicknesses (<100 nm) calculated for the corresponding Cr/Al-rich primary corrosion protection. Most of the alloys exposed in the TGA showed no, or very short (<1 h), incubation times to breakaway, with the exceptions being the Fe18Cr, Fe18Cr2Ni and Fe18Cr5Ni alloys as previously described.

For the first set of model alloys (FeCr), only minor effects were

observed upon increasing the chromium content from 2.25 to 18 wt% Cr. A rapid reduction in growth rate was observed at 25 wt% Cr. However, the growth kinetics of this oxide scale was very different from the other alloys, suggesting that the sample remained in the primary corrosion regime. Thus, this oxide should not be considered in the analysis of the secondary corrosion regime.

For the second set of model alloys (FeCrNi) the mass gains were observed to decrease rapidly when the amount of Ni reached 5 wt% Ni, and remained almost constant as the amount was further increased (5–34 wt% Ni). Note that the FeCrNi system contained alloys with different crystal structures (BCC/FCC). Thus, as the amount of Ni was increased, the alloy crystal structure also changed from BCC to FCC (see Table 1).

The third set of model alloys (FeCrAl) showed a linear reduction (mg/cm<sup>2</sup> ∝ wt% Al) in growth rate as the amount of Al increased from 0 to 3 wt%. Note that the Fe18Cr6Al alloy did not break down in the presence of K<sub>2</sub>CO<sub>3</sub> (also after 168 h exposure) but exhibited a mass gain corresponding to an estimated thickness of approximately 100 nm. Thus, this oxide remained in the primary corrosion protection and should not be considered in the analysis of the secondary corrosion regime.

As the amount of Cr increased in the FeCrAl alloys, the mass gains were observed to be similar for 5–10 wt% Cr while a rapid reduction in growth rate was observed between 10 and 18 wt% Cr. The oxide growth rate remained comparatively low also on the FeCrAl alloy containing 25 wt% Cr (Fe25Cr3Al).

## 3.2. Microstructure and composition

### 3.2.1. Oxide formed in mild environments – primary corrosion regime

The results from the SEM/EDX plan view investigation of the primary corrosion protection were in line with the mass gain data indicating a homogeneous, thin, Cr-rich oxide scale on all samples exhibiting low mass gains, with metal grains visible through the oxide, see representative examples in Fig. 4a. The visible metal grains indicated that the thickness was thinner than the interaction volume of BSEs, which is in good agreement with the estimated thicknesses calculated from mass gains. A thicker Fe-rich oxide was observed on the alloy with 5 wt% Cr (Fe5Cr3Al), see Fig. 4b, explaining the higher mass gain. The FeCrNi alloy with 20 wt% Ni (Fe18Cr20Ni) also formed a thicker Fe-rich oxide scale on several alloy grains, see Fig. 4c, indicating that breakaway had been initiated. Thus, the thickness estimated from mass gain data is not expected to agree well with the actual thickness of the oxide formed in this sample. The FeCrNi alloy with 34 wt% Ni (Fe18Cr34Ni) formed a thin Cr-rich oxide on the alloy grain boundaries and a thicker Fe-oxide on the alloy grains (see Fig. 4d). It should be noted that the compositions of the thin oxides were not possible to quantify with EDX since the interaction volume of the EDX covers both the oxide and the alloy underneath. Thus, only qualitative compositions are mentioned. No cross sections were prepared of the oxide scales formed in the primary

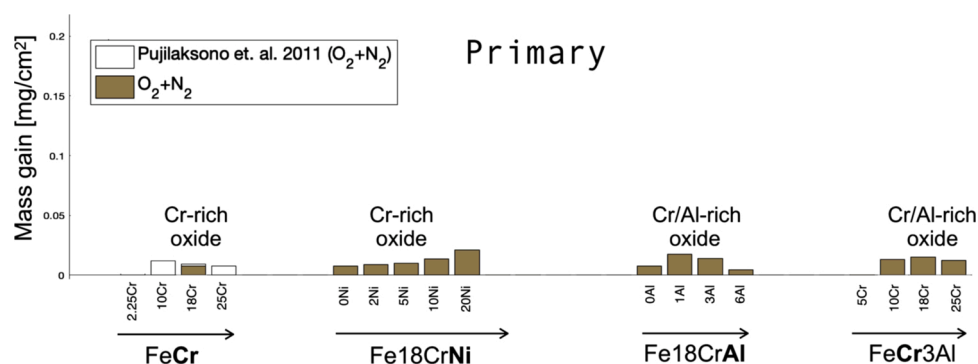


**Fig. 2.** Mass gains observed for FeCr, FeCrNi and FeCrAl model alloys exposed for 24 hrs in 5% O<sub>2</sub> + 95% N<sub>2</sub> at 600 °C representing a mild environment in order to study the primary corrosion protection.



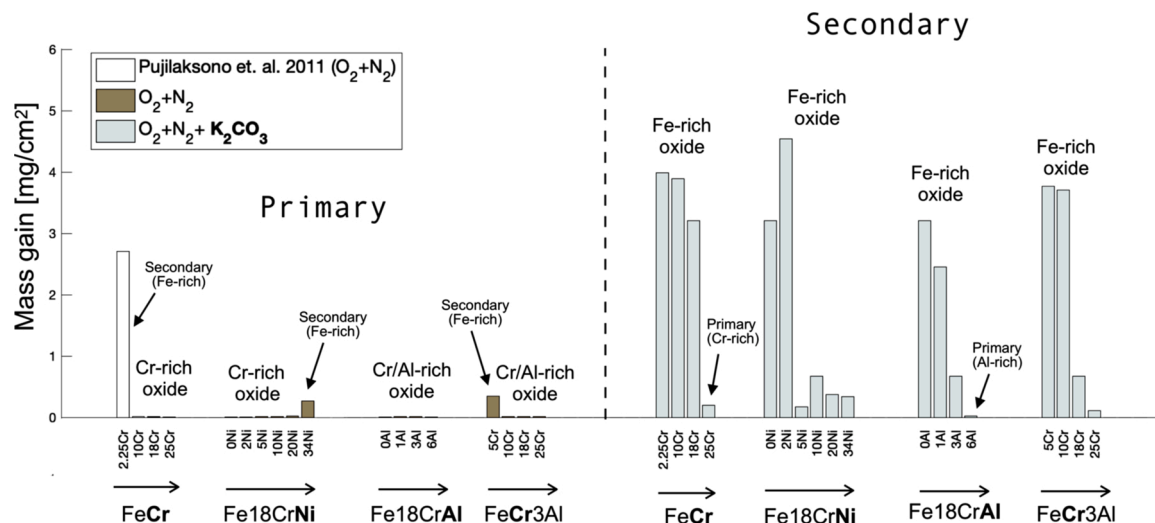


**Fig. 3.** (a) Mass gains for FeCr, FeCrNi and FeCrAl model alloys exposed for 24 hrs in 5%  $O_2 + 95\%$   $N_2$  at  $600^\circ C$  with and without  $K_2CO_3$  deposited prior to exposure. Note that the exposures without  $K_2CO_3$  (primary corrosion protection) were performed in a tube furnace while the  $K_2CO_3$  exposures (secondary corrosion regime) were performed in the TGA to exclude eventual variations in incubation time.

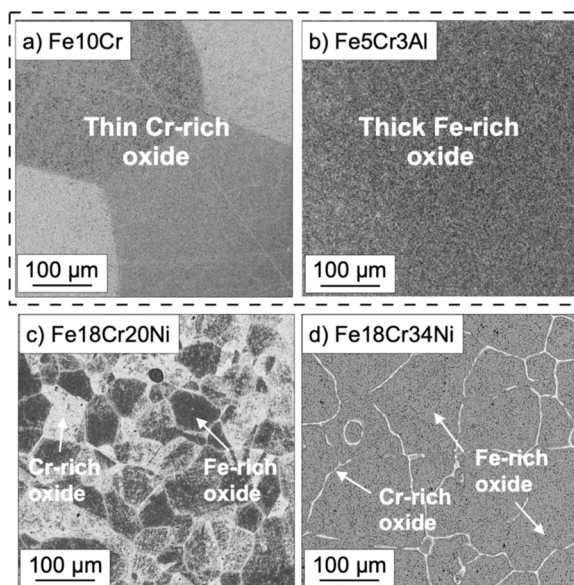


**Fig. 4.** Plan view BSE-SEM images of the type of oxide scales that formed after 24 h exposure in 5%  $O_2 + 95\%$   $N_2$  at  $600^\circ C$ . The thin Cr/Al-rich scale (a) was observed on the majority of the exposed model alloys, while the Fe-rich oxide (b) was observed on parts of the surfaces of the alloys with low Cr content (Fe2.25Cr [20], Fe5Cr3Al) and on several alloy grains on the Fe18Cr20Ni (c). The Fe18Cr34Ni alloy (d) formed Fe-rich oxide on the alloy grains and a thinner Cr-rich oxide on top of the alloy grain boundaries.

corrosion regime, since the focus of the microstructural investigation was on the secondary corrosion regime.

### 3.2.2. Oxide formed in harsh environments – secondary corrosion regime

The oxide scales formed after breakaway oxidation (secondary corrosion regime) were investigated in detail by SEM/EDX on mm wide ion milled cross-sections after 48 h of exposure. The calculated thicknesses were in good agreement with the measured thicknesses. A representative selection of samples for each set of model alloys are shown in Fig. 6a–d.

The microstructural investigation showed that, independently on growth rate and alloy composition, all oxide scales formed a similar

microstructure, composed of a multi-layered oxide scale and a region of internal oxidation at the scale/metal interface, which is represented schematically in Fig. 5. The microstructure suggest that the internal oxidation was of reaction zone-type (RZ) on the majority of the samples, meaning a region with mixed spinel type oxide and metal [37]. No indications of formation of a healing layer (re-formation of the primary corrosion protection) could be observed with the SEM/EDX on any of the alloys. However, since the resolution of the SEM/EDX is in the range of  $\mu m$  this needs to be investigated at higher spatial resolution with, e.g. STEM/EDX.

The composition of the multi-layered oxide scales, as analyzed by SEM/EDX, are summarized in Table 3. The oxide scales were composed

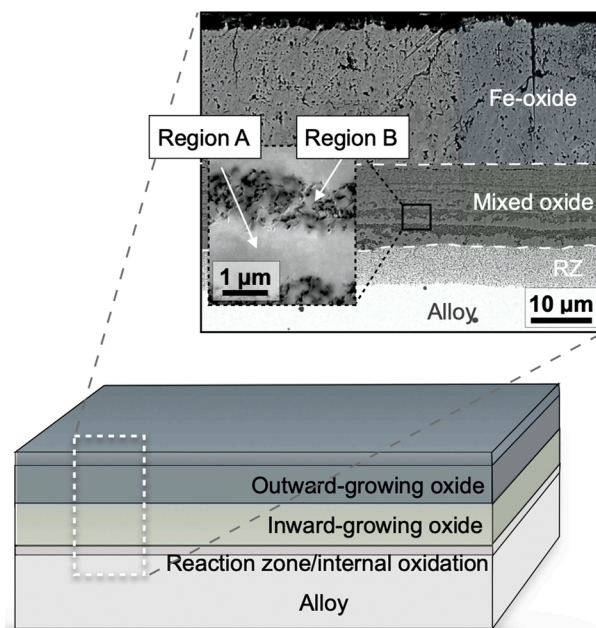


**Fig. 5.** Example of the oxide scale formed in the secondary regime on Fe-based alloys at  $600^\circ C$ . The oxide scale is composed of outward-growing iron oxide ( $Fe_2O_3/Fe_3O_4$ ) and an inward-growing mixed (Fe, Cr, Al/Ni) oxide. The inward-growing oxide typically has a banded microstructure with alternating bright (region A) and dark (region B) contrast and a reaction zone type of internal oxidation at the scale/metal interface.

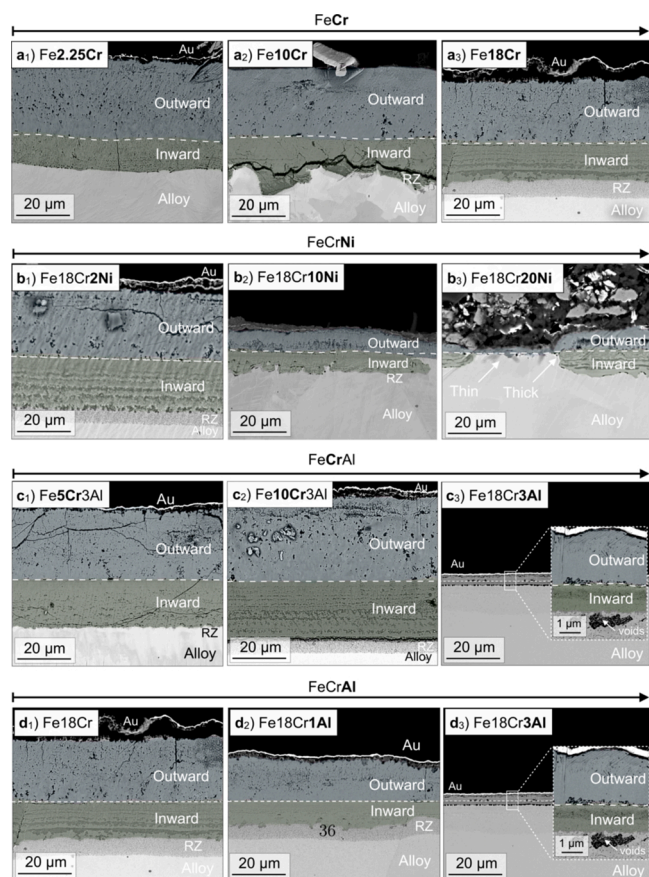


**Fig. 6.** BSE-SEM images of the oxide scales formed after 48 h exposure in 5%  $O_2 + N_2 + 1$  mg  $K_2CO_3(s)$  at 600 °C on (a) FeCr, (b) FeCrNi, (c,d) FeCrAl alloys. The different types of layers are falsely colored (post-processed) to simplify for comparisons between the oxide layers formed on different alloys. A region of internal oxidation is indicated by the majority of the samples, where the most common type is the reaction zone (RZ).

of an outward-growing, almost pure, iron oxide and an inward-growing oxide containing a mixture of Fe, Cr, Al/Ni. All alloying elements, apart from Fe and small amounts (<2%) of Cr, remained in the inward-growing oxide on all exposed alloys. Note that the interaction volumes of the SEM/EDX result in composition from volume in the micrometer range, resulting in that the reported composition is an average composition from this volume.

The inward-growing oxides formed a banded structure with alternating bright and dark regions, apparent on all the thick oxide scales and indicated on the thinner Fe-rich oxide scales (one period of alternation). The brighter regions in the inward-growing oxide (region A) were dense and appeared to be fully oxidized while the darker regions (region B) were porous. Both types of regions were depleted in iron even though the porous region B was observed to be more depleted in iron, and enriched in Cr, compared to the fully oxidized region A (see Table 3). The porous bands (region B) were in between 0.5 and 2 µm in thickness and estimated to 30–40% of the cross-sectional area observed in the microstructural investigating (see Fig. 6 and 5). The bands were observed to be thicker and alternations less frequent closer to the alloy interface, compared to the outward/inward oxide interface. The amount of porous region B compared to dense region A was similar for all alloys clearly exhibiting the banded structure.

The overall influence of alloying elements observed in the gravimetric results were validated in the microstructural investigation for each exposed set of model alloys (see Fig. 6). Fig. 6a<sub>1</sub>–a<sub>3</sub> shows that the addition of Cr (from 2.25 to 18 wt% Cr) had little effect on the final oxide scale thickness on the FeCr alloys in similarity to the FeCrAl alloys

**Table 3**

Cationic composition (SEM/EDX results in at%) of the outward and inward-growing scales formed on the model alloys exposed for 48 h at 600 °C to 5%  $O_2 + 95\% N_2$  in the presence of  $K_2CO_3$ . The inward-growing scale comprises two types of regions (Region A and Region B; see Fig. 5). Note that the interaction volume for the acquired data in \* is expected to partly cover both Region A and B, as well as \*\* the alloy beneath the oxide scale.

FeCr alloys	Outward-growing		Inward-growing	
	Fe	Cr	Fe	Cr
Fe2.25Cr	bal.	<1	bal.	6–9 (15 at M/O interface)
Fe10Cr	bal.	<1	bal.	25–30
Fe18Cr	bal.	<2	bal.	43 (A:39–41, B:45–48)*
Fe25Cr	–	–	–	–

FeCrNi alloys	Outward-growing			Inward-growing		
	Fe	Cr	Ni	Fe	Cr	Ni
Fe18Cr(0Ni)	bal.	<2	–	bal.	43 (A:39–41, B:45–48)*	–
Fe18Cr2Ni	bal.	<2	0	bal.	(A:37–39, B:46)*	2–3
Fe18Cr5Ni	bal.	<2	0	bal.	44–46	4–6
Fe18Cr10Ni	bal.	<2	0	bal.	35–38	8–18
Fe18Cr20Ni	bal.	<1	0	bal.	(A:29–30, B:44–45)*	(A:39–42, B:17–19)*

FeCrAl alloys	Outward-growing			Inward-growing		
	Fe	Cr	Al	Fe	Cr	Al
Fe5Cr3Al	bal.	–	–	bal.	–	–
Fe10Cr3Al	bal.	<1	<1	bal.	20–22	14–15
Fe18Cr3Al*	bal.	4–9	1–3	bal.	(A:29–32, B:50–51)*	11–13
Fe25Cr3Al*	bal.	23–29	1–2	bal.	55–59	13–14
Fe18Cr(0Al)	bal.	<2	–	bal.	43 (A:39–41, B:45–48)*	–
Fe18Cr1Al	bal.	<2	<1	bal.	39	5–
Fe18Cr3Al*	bal.	4–9	1–3	bal.	(A:29–32, B:50–51)*	11–13

with low Cr content (2.25–10 wt% Cr) (see Fig. 6c<sub>1</sub>–c<sub>2</sub>). However, increasing the amount of Cr from 10% to 18% resulted in a rapid reduction in oxide scale thickness on the FeCrAl alloys, with a thickness that remained almost constant as the amount of Cr was further increased (Fe25Cr3Al) (see Fig. 6c<sub>2</sub>–c<sub>3</sub>). It should be noted that the FeCrAl alloys with high Cr content (Fe18Cr3Al, Fe25Cr3Al) showed alloy microstructures, possibly indicating nitridation (compare Fig. 6c<sub>3</sub> to nitridation zone in, e.g. [36]) as well as a region containing larger voids at the scale/metal interface (see Fig. 6c<sub>3</sub>). Al-rich oxides may be misinterpreted in the SEM as voids due to contrast mechanisms. This was taken into consideration by sample tilting in the SEM, using the edge effect of secondary electrons and the knowledge of the position of the EHT-detector, to conclude that these structures were voids.

The oxide scales shown in Fig. 6b<sub>1</sub>–b<sub>3</sub>) also agreed well with the gravimetric results, showing thicker oxide scales on the alloys with low amounts of Ni with a rapid reduction in oxide scale thickness between 2 and 10 wt% Ni and no significant influence as the amount of Ni was further increased. Note that the scale formed on the FeCrNi alloys grew less homogeneously over the sample surface than the FeCr and FeCrAl alloys (see Fig. 6a, c and d). The difference in thickness observed could not be concluded to be related to specific alloy grains nor alloy grain boundaries.

The oxide scale formed on FeCrAl alloys with varying amounts of Al was also reduced in thickness as the amount of Al was increased (see Fig. 6d<sub>1</sub>–d<sub>3</sub>) in good agreement with the gravimetric results.

Fig. 7 shows the measured thicknesses of inward- and outward-growing oxides for all exposed alloys, as well as the calculated thicknesses based on mass gain data. The total thicknesses were in good agreement with the gravimetric results (48 h) for most of the alloys. The relative amounts of outward- and inward-growing scales are shown in Fig. 8 and summarized in Table 4. The outward-growing iron oxides had



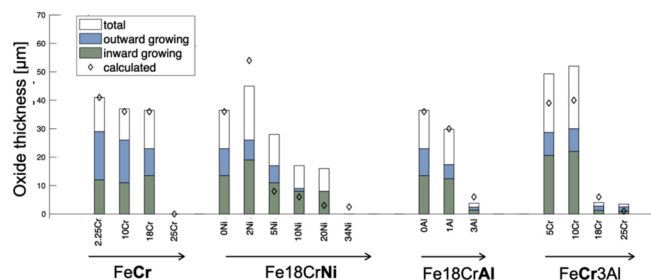


**Fig. 7.** Summary of the measured oxide scale thicknesses for all model alloys exposed for 48 h in 5%  $O_2 + 95\% N_2 + 1 \text{ mg } K_2CO_3(s)$  at  $600^\circ$ , including the estimated thicknesses calculated from mass gain data ( $\diamond$ ). Note that the oxide scale formed on the Fe18Cr34Ni alloy was not examined in cross section.

thicknesses corresponding to approximately 60–70% of the total oxide scale while the inward-growing oxides were on average 30–40% for all exposed alloys, except for Fe18Cr20Ni (in:out = 50:50). Note that neither the variation in alloy composition nor growth rate had a considerable impact on the relative amount of inward- and outward-growing oxides.

The diffusion of charged species through the scale could be largely affected by the presence of short-circuit diffusion paths, such as oxide grain boundaries. Thus, the oxide grain size (i.e. the amount of grain boundaries) of the outward- and inward-growing oxide were measured on a selection of samples (see Table 4). Fig. 9 shows the oxide grains of the outward(a) and inward(b) growing oxides formed on a few selected model alloys after 48 h of exposure. The samples were chosen for comparison due to the formation of oxides with different growth rates ( $a_1, b_1$ : thick oxide scales,  $a_2, b_2$ : thin oxide scales). The oxide grain size of the outward-growing oxide (see Fig. 9a) were measured to be approximately  $1 \mu m$  for Fe18Cr2Ni( $a_1$ ) and  $150 \text{ nm}$  for Fe18Cr10Ni( $a_2$ ). Combining these observations with the overall thicknesses of these scales (45 and  $14 \mu m$  respectively) it could be concluded that the largest grains were present on the thicker, fast-growing, oxide scales. The same trend was observed for the inward-growing oxide (b), showing larger grains on the fast-growing scale (avg.  $500 \text{ nm}$  ( $b_1$ )) and smaller on the slow-growing ( $300 \text{ nm}$ , ( $b_2$ )). It should be noted that a variation in grain size was observed throughout both the outward- and inward-growing scales, see, e.g. the inward-growing oxide in Fig. 9b<sub>1</sub> at the interface to the outward-growing oxide where columnar grains of approximately  $100 \text{ nm}$  width were observed.

#### 4. Discussion

The corrosion mechanisms before and after breakaway are in considered to be fundamentally different (see Fig. 1). Thus, the discussion below is separated for the primary (before breakaway) and the

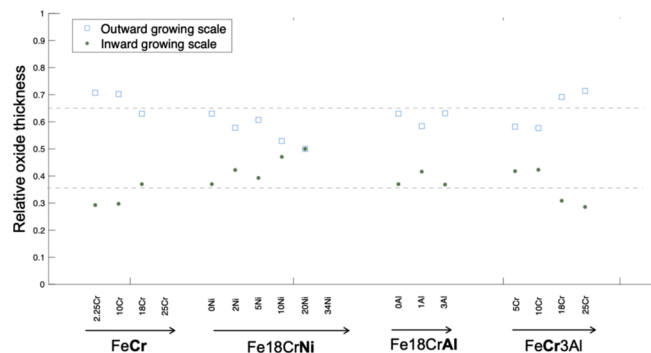


**Fig. 8.** Summary of the relative amounts of inward- and outward-growing scales for all model alloys in the secondary corrosion regime (exposed for 48 h in 5%  $O_2 + N_2 + 1 \text{ mg } K_2CO_3(s)$  at  $600^\circ$ ).

**Table 4**

Oxide scale thicknesses, relative amounts of inward- and outward-growing scales and oxide grain sizes of the oxide scales formed on the FeCr(Ni/Al) model alloys with varying amounts of Cr, Ni or Al after 48 h exposure to 5%  $O_2 + 95\% N_2$  at  $600^\circ C$  in the presence of  $K_2CO_3$ . Note that some of the oxide scales studied were exposed for 24 h in a regular tube furnace. Due to difficulties separating hematite and magnetite in the micrographs it is assumed that the grains measured in the outward-growing scale are magnetite grains.

Alloy	Thickness [ $\mu m$ ]	Out [ $\mu m$ ]	In [ $\mu m$ ]	Out: In [%: %]	Grain size Out [nm]	Grain size In [nm]
<i>FeCr alloys</i>						
Fe2.25Cr	41	29	12	70:30	700 (500–900)	500 (100–500)
Fe10Cr	37	26	11	70:30	750	250
Fe18Cr	37	23	14	62:38	1000	–
Fe25Cr	–	–	–	–	–	–
<i>FeCrNi alloys</i>						
Fe18Cr(0Ni)	37	23	14	62:38	1000	–
Fe18Cr2Ni	45	26	19	58:42	1000	–
Fe18Cr5Ni	28	17	11	61:39	200	300
Fe18Cr10Ni	17	9	8	53:47	150	100
Fe18Cr20Ni	16	8	8	50:50	200	–
Fe18Cr34Ni	–	–	–	–	–	–
<i>FeCrAl alloys</i>						
Fe5Cr3Al	50	29	21	58:42	–	–
Fe10Cr3Al	52	30	22	58:42	850	–
Fe18Cr3Al	4	2.5	1.5	62:38	–	–
Fe25Cr3Al	3.5	2.5	1	71:29	–	–
Fe18Cr(0Al)	37	23	14	62:38	1000	–
Fe18Cr1Al	30	18	12	60:40	–	–
Fe18Cr3Al	4	2.5	1.5	62:38	–	–
Fe18Cr	20	12	8	60:40	450	–
(0Al), 24 h						
Fe18Cr1Al,	16	10	6	62:38	275	–
24 h						
Fe18Cr3Al,	3	2	1	60:40	200	–
24 h						

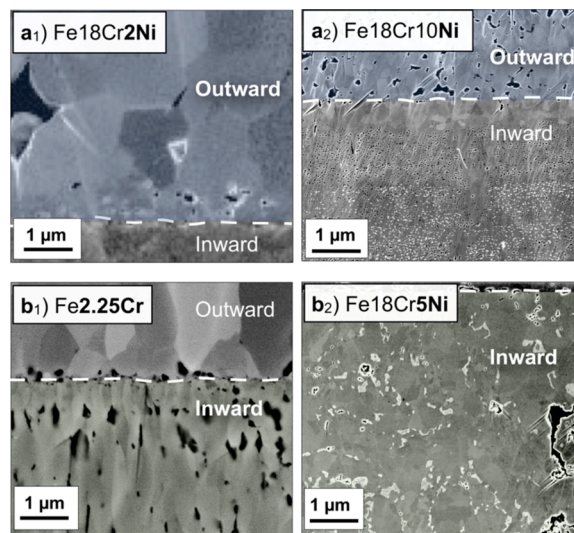


**Fig. 9.** Ion induced SE( $a_1$ ) and low keV BSE( $a_2, b_1$ – $b_2$ ) images showing the oxide grains of the outward ( $a_1$ – $a_2$ ) and inward ( $b_1$ – $b_2$ ) growing oxides formed on fast and slow growing oxide scales after 48 h exposure in  $1 \text{ mg/cm}^2 K_2CO_3 + 5\% O_2 + 95\% N_2$  at  $600^\circ C$ . The grain sizes are larger in the thicker oxide scales ( $a_1, b_1$ ) compared to the thinner ( $a_2, b_2$ ) for both the inward and outward-growing oxides. Note that there is a variation in grain size throughout the scales.



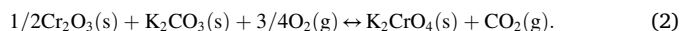
secondary (after breakaway) corrosion regimes.

#### 4.1. Primary corrosion regime

It is well known that the corrosion protection of stainless steels and FeCrAl alloys exposed in mildly corrosive environments rely on the formation of a slow-growing Cr-rich or Al/Cr-rich  $M_2O_3$  oxide scale, i.e. the primary corrosion protection [1–3]. The amounts of Cr and Al in low alloyed steels are not sufficient to form the primary corrosion protection. Thus, low alloyed steels only form the Fe-rich type of oxide scale (i.e. the secondary corrosion regime). This is in good agreement with the results from this study, showing that most of the samples formed a slow-growing Cr/Al-rich oxide scale in the mild exposure environment ( $O_2 + N_2$ ) with the exception being the alloys with low Cr content (Fe2.25Cr [20], Fe5Cr3Al) and the alloy with 34 wt% Ni (Fe18Cr34Ni) (see Fig. 2 and 4). The results from this study also indicate that the primary corrosion protection of FeCrAl alloys ( $(Al,Cr)_2O_3$ ) act similar to the Cr-rich type of oxide scale at intermediately high temperatures, e.g. 600 °C, in good agreement with recent investigations [35,40]. The oxidation of stainless steels and FeCrAl alloys before and after breakaway have previously been studied extensively [5–10,12–29]. The previous studies show that a variation in Cr, Al or Ni in the alloy have minor influence on the growth rate of the primary corrosion protection ( $Cr_2O_3$ ,  $Al_2O_3$ ) in relation to the fast-growing Fe-rich oxide scale formed after breakaway (see, e.g. [20]). The results from this study are in line with these observations, showing scales with calculated thicknesses of <100 nm, with small influence of alloy composition, on the materials forming a primary corrosion protection of Cr/Al-rich oxide. A small improvement in the primary corrosion protection could be observed when alloying with Al while the mass gain increased slightly with the addition of Ni (0–10 wt%). Note that the alloys with low Cr content (Fe2.25Cr [20], Fe5Cr3Al) and the 34 wt% Ni alloy (Fe18Cr34Ni) do not form a primary corrosion protection under the studied conditions, but an Fe-rich oxide scale, similar to the oxide scale formed in the presence of  $K_2CO_3$  (in the secondary corrosion regime).

#### 4.2. Breakaway oxidation – transition from primary to secondary corrosion regimes

The Cr-rich  $M_2O_3$  scale provides a slow-growing protection of the alloy at intermediately high temperatures (e.g. 600 °C). However, in more corrosive environments the Cr-rich oxide breaks down and a fast-growing multi-layered Fe-rich oxide forms (see Fig. 1) [5–35]. Jonsson et al. [37] showed that several different corrosion environments gave similar oxide microstructure after breakaway at 600 °C. J. Pettersson et al. [11,19] studied the influence of different alkali containing species on the breakdown of the Cr-rich oxide scale (i.e. primary corrosion protection). The study showed similar corrosion behavior in presence of KCl and  $K_2CO_3$ , and proposed the breakdown to be caused by a mechanism where K reacts with Cr in the  $M_2O_3$  scale to form potassium chromate (see, e.g. reaction (2)) [11]:



In this study the breakdown of the primary corrosion protection is induced by the presence of  $K_2CO_3$  in order to study the oxidation of the secondary corrosion regime without including possible influence of other corrosive species such as, e.g. Cl [19]. The results show that the presence of  $K_2CO_3$  breaks down the primary corrosion protection on all alloys forming the thin Cr/Al-rich oxide scales as its primary corrosion protection, except for the Fe18Cr6Al (also after 168 h), see Fig. 2. This indicates that the higher amount of Al changes the character of the primary corrosion protection from acting more similar to the Cr-rich  $M_2O_3$  (breaking down in the presence of  $K_2CO_3$ ) to sustain its protective properties in the presence of  $K_2CO_3$  (more Al-rich  $M_2O_3$ ).

The breakdown of the primary corrosion protection of FeCrNi alloys

has previously been studied by several authors (see, e.g. [6,9,27,41,42]). Peraldi and Pint [9] and R.F.A. Pettersson et al. [41,42] studied the influence of Ni at higher Ni contents (10–30 wt% Ni and 14–78 % Ni respectively) in presence of water vapor at 650–800 °C. The results from both studies indicated that Ni has a beneficial effect on the Cr-rich oxide scale (i.e. primary corrosion protection) and delayed the formation of a thicker Fe-rich oxide scale (i.e. secondary corrosion regime) also in more complex environments (e.g. in presence of HCl or  $SO_2$  [42]). In contrary, the results from this study shows that the incubation time to breakaway is very short (<1 h) for all exposed alloys except for the alloys with low Ni content (Fe18Cr, Fe18Cr2Ni alloys (<6 h) and the Fe18Cr5Ni ~ 20 h). Nevertheless, the short incubation times observed in this study, indicate that the oxide scales analyzed after 48 h of exposure are good representatives for trends in how the secondary corrosion regime is influenced by altering the alloy composition.

#### 4.3. Secondary corrosion regime

##### 4.3.1. General remarks

The gravimetric results, in combination with the microstructural investigation performed in this study, show that the growth rate after breakaway may be greatly influenced by the change in alloy composition for certain alloys (see Figs. 3 and 6) in good agreement with previous studies (see, e.g. [9,36]). Thus, independent on how well the primary corrosion protection withstands the environment, the corrosion resistance of a material exposed in a harsh environment could be improved by optimizing the protective properties of the Fe-rich oxide scale formed after breakaway, i.e. the secondary corrosion protection.

The oxide scale formed after breakaway, i.e. in the secondary corrosion regime, has previously been studied in several different environments (see, e.g. [4,39,10,20,21,24,25,27,37,38]). Jonsson et al. [37] showed that the environment had limited influence on the microstructure formed after breakaway oxidation. It was suggested that the microstructure was caused by a diffusion controlled process explained by the different diffusivities of cations in the inward-growing spinel. This is in good agreement with the results from the microstructural investigation performed in this study, suggesting that the microstructural evolution of the oxide scale formed in the secondary corrosion regime is based on diffusion on both FeCr and FeCrNi, as well as FeCrAl alloys (see Fig. 6). Thus, the growth of the oxide scales formed in the secondary corrosion regime could be modeled similarly for several Fe-based alloys with the help of modeling tools such as, e.g. DICTRA [4,39]. Note that this observation does not prove that diffusion is the rate limiting factor in the growth process. However, many previous studies, on multi-layered Fe-rich oxides, similar to those observed in this study, have shown nearly parabolic kinetics, indicating diffusion controlled growth (see summaries in, e.g. [43] and [44]).

The diffusivity of Fe in the spinel phase has been shown to be much higher than that of Cr, Al and Ni [45,46] (see diffusivities in magnetite in Fig. 10, reproduced from data in [45,46]). Even though the data was attained at higher temperatures (~1200 °C), than the exposure temperature in this study, the differences are in good agreement with the observed results. Thus, provided that the growth is based on diffusion, this may be used to explain why the outward-growing oxides are composed of almost pure iron oxide while the other alloying elements (Cr,Al/Ni) remain in the inward-growing oxide scale.

Furthermore, the results in this study suggest that the oxide scales are composed of an outward-growing Fe-oxide, with a thickness corresponding to 60–70% of the total oxide scale, and an inward-growing oxide with a thickness of approximately 30–40% of the total oxide scale (see Fig. 7). This is observed on all exposed Fe-based alloys, except for the Fe18Cr20Ni alloy, which form an oxide scale with the same amount of in- and outward-growing oxides. The relative amount of inward- and outward-growing oxide remain similar for both slow-growing (thin) and fast-growing (thick) scales (see Fig. 7). In general terms, the similar ratios of inward- and outward-growing scales indicate that the

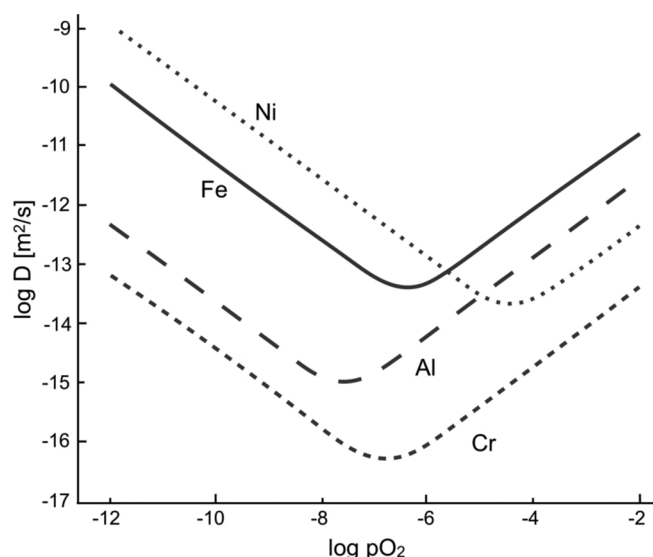


Fig. 10. Diffusion coefficients of cations (Fe, Cr, Al, Ni) in  $\text{Fe}_3\text{O}_4$  at 1200 °C. Data for reconstructing the figure was reported by Dieckmann and Schmalzried [53] and summarized by Van Orman and Crispin [46].

full oxide scale is up-scaled, and that not only one of the oxides is influenced as the alloy composition and growth rate is changed. The outward- and inward-growing scales are expected to form either by outward diffusion of cations (outward-growing scales) or inward diffusion of anions (inward-growing scale) [1]. Bertrand et al. [47] studied the multi-layered iron oxide scale formed on pure iron (<570 °C) by  $\text{O}^{16}/\text{O}^{18}$ -tracer experiments showing that the outward growing hematite and magnetite layers formed by cation outward diffusion and that the inner, inward-growing magnetite formed by oxygen inward diffusion. Thus, the nearly constant ratios of inward- and outward-growing scales observed in this study indicate that both anion inward diffusion ( $\text{O}^{2-}$ ) and cation outward diffusion ( $\text{Fe}^{2+}/\text{Fe}^{3+}$ ) are affected to a similar extent as the alloy composition is changed. However, it is probable that the different ionic currents are linked and that the influence of one ionic current could affect the ionic currents in the opposite direction. Previous studies on duplex oxide scales have explained the constant ratio of inward- and outward-growing scales by “the available space model” see, e. g. Gibbs et al. [48] or Martinelli et al. [49]. The model is based on that the growth of the inward-growing spinel is linked to the outward diffusion of iron by that it grows in the available space created by vacancies in the alloy formed as a result of outward diffusion of iron. Thus, according to this model, an enhanced outward diffusion of iron would result in a proportional increase in inward-growing scale. The results from this study (with similar ratios of inward- and outward-growing scales for all the  $\text{K}_2\text{CO}_3$ -exposed model alloys, see Fig. 8)) indicate that neither the alloy composition nor alloy microstructure affects the linked relation between the in- and outward-growing scales considerably. Thus, if the outward diffusion of iron would result in an inward-growing scale for any alloy composition, the protective properties of the formed inward-growing scale, specifically possible reductions in Fe-diffusion, in the inward-growing spinel would be of major importance for the growth rate of the full oxide scale.

The change in alloy composition results in altered properties of the formed oxide scales as well as a variation in the alloy microstructure. In order to better explain the observed differences in growth rate and understand what parameters that could determine the protective properties in the secondary corrosion regime a few potential aspects are discussed in detail regarding **alloy microstructure** as well as **oxide microstructure** and **chemical composition** of the outward- and inward-growing scales.

#### 4.3.2. Alloy microstructure

The alloy microstructure is well known to influence oxidation properties of metallic materials. The exposed alloys in this study have different grain sizes as well as crystal structures (BCC/FCC) (see Table 1). Both these factors may be important aspects to understand the oxide growth rate since they both may influence, e.g. the diffusion of charged species to the surface.

**Alloy grain size:** The investigated alloys in this study exhibited different grain sizes (see Table 1). It is well known that the alloy grain size may influence oxidation kinetics by that grain boundary diffusion is faster than lattice diffusion at intermediate temperatures (~600 °C) [50]. Thus, more alloy grain boundaries, i.e. faster cationic transport through the alloy, would result in a more rapid recovery from depletion of alloying elements at the corrosion front. However, in this study a very small difference in incubation times are observed (independent on alloy grain size) indicating that the diffusion rate of, e.g. Cr to the surface is not the rate limiting factor.

Furthermore, by comparing the alloy grain sizes with the overall growth rates after breakaway (secondary corrosion regime) it can be concluded that the amount of alloy grain boundaries cannot alone explain the change in growth rate observed in this study, since larger alloy grains are both observed on alloys exhibiting fast as well as slow oxide growth (compare Fig. 3 and Table 1).

**Crystal structure:** Regarding the crystal structure, alloying elements, such as Cr, Ni, Fe and O, are known to diffuse faster in ferritic steels (BCC) compared to austenitic steels (FCC). Thus, depletion of alloying elements at the corrosion front, caused by oxidation or other reactions with the surrounding atmosphere, is expected to be less in ferritic steels. It should be noted that the SEM/EDX analysis in this study was mainly performed by several point analysis of the specified regions (inward-growing scale, outward-growing scale, alloy), and line-scans were only performed on a few alloys. Thus, no depletion zones were detected in this study. Further chemical analysis with better spatial resolution is required to conclude if depletion zones are present in the alloy below the oxide scale.

The FeCrNi matrix investigated in this study changes crystal structure (from BCC, via duplex BCC/FCC, to FCC) as the amount of Ni is increased (see Table 1), since Ni stabilizes the austenite phase (FCC). The results from this study shows that an increased amount of Ni in the alloy is beneficial for the secondary corrosion protection up to approximately 5 wt%, after which Ni does not influence the growth rate significantly. However, since the rapid decrease in growth rate observed in this study may be partly explained by the two different crystal structures, exhibited by the alloys below (BCC) as well as above (FCC) 5 wt% Ni, the direct influence of Ni in the secondary corrosion regime should be handled with caution. Peraldi and Pint [9] studied the corrosion of austenitic and duplex (BCC/FCC) FeCrNi model alloys with higher amounts of Ni (10–30 wt% Ni) in presence of water vapor, indicating a beneficial effect of Ni both regarding the transition to the secondary corrosion regime (650 °C) and the resistance to spallation (850 °C). Further studies are ongoing to investigate the influence of Ni and crystal structure on the secondary corrosion protection in more detail.

#### 4.3.3. Outward-growing oxide

**Microstructure:** The oxide grain size of the outward-growing scales in this study are observed to vary for the different alloy compositions, with oxide grains ranging from approximately 100 nm to 1  $\mu\text{m}$  (see Fig. 9a). The results indicate a trend in larger grain size for thicker oxide scales. The average grain sizes of the oxides formed on a selection of alloys are summarized as a function of oxide scale thickness in Fig. 11a, showing that larger oxide grains (i.e. less grain boundaries) are observed on the thicker oxide scales. Diffusion of both anions (e.g.  $\text{O}^{2-}$ ) and cations (e.g.  $\text{Fe}^{2+/3+}$ ,  $\text{Cr}^{3+}$ ,  $\text{Al}^{3+}$ ,  $\text{Ni}^{2+}$ ) along oxide grain boundaries are in general considered to be faster diffusion paths than lattice diffusion at

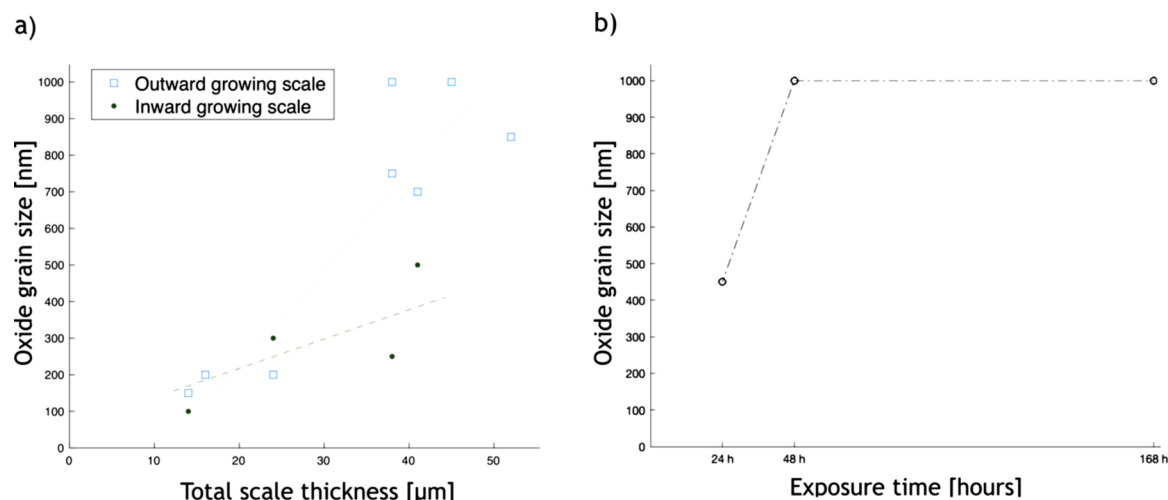


**Fig. 11.** Grain size of (a) inward and outward-growing oxides as a function of total oxide scale thickness for several alloys exposed for 48 h and (b) outward-growing oxide formed on Fe18Cr exposed in 1 mg/cm<sup>2</sup> K<sub>2</sub>CO<sub>3</sub> + 5% O<sub>2</sub> + 95% N<sub>2</sub> at 600 °C. The trend-lines in (a) shows that the grain sizes are larger on the thicker oxide scales while (b) shows that grain growth is evident up to 48 h in the outward-growing oxide formed on Fe18Cr.

intermediately high temperatures (e.g. 600 °C) [50]. Thus, the observations of smaller oxide grains, i.e. higher density of grain boundaries, in the slow-growing oxide scales indicate that faster grain boundary diffusion does not alone determine the overall growth rate of the oxide scale.

However, it should be noted that a difference in grain growth for oxides with different thicknesses are to be expected in a multi-layered scale, since each oxide layer may have existed for different amounts of time. Thus, processes such as grain growth, well known to occur in iron oxides at 600 °C (see, e.g. [51]), should be considered. The oxide grain growth was studied briefly on the outward-growing oxide on the Fe18Cr alloy at 24, 48 and 168 h (see Fig. 11b) showing a considerable grain growth in between 24 and 48 h of exposure. Thus, grain growth should be considered and studied in further detail before making further conclusions.

**Chemical composition:** The results show that the chemical composition of the outward-growing oxide is very similar for all the model alloys. The outward-growing oxide is almost pure iron oxide with small amounts of Cr (<2% detected by SEM/EDX.) Thus, the dramatic changes in oxide growth rate, indicating a secondary corrosion protection, is proposed not to be explained by the variation in composition of the outward-growing oxide, but instead possibly by the changes in the inward-growing oxide scale.

#### 4.3.4. Inward-growing oxide

**Microstructure:** The oxide grain size of the inward-growing spinel showed the same trend as in the outward-growing oxide, with a smaller average oxide grain size (~300 nm) on the slow-growing oxide scales compared to the fast-growing (~500 nm) (see Fig. 9b). Thus, faster grain boundary diffusion in the inward-growing scale, is also suggested not to alone determine the secondary corrosion protection at 600 °C. It should be noted that the oxide grains were difficult to image in the inward-growing scale on several samples due to the complex and porous microstructure of this oxide scale.

In the secondary corrosion regime, most alloys show indications of internal oxidation at the scale/metal interface. The microstructure suggests it to be of type reaction zone (i.e. spinel type oxide precipitates in a metal matrix) for all exposed alloys except for the Fe18Cr3Al and Fe25Cr3Al, instead forming larger voids in this region. Previous studies performed on FeCr [25,37] and FeCrNi [37,26,27] alloys showed that the reaction zone was composed of Cr-rich oxide precipitates and Cr-depleted metal. The oxide precipitates were concluded to be of spinel type and the reaction zone was explained by a miscibility gap present in

both the FeCr and FeCrNi system at 600 °C. The microstructure, of the reaction zone observed in this study, is very similar to those observed in the previous studies. Thus, it is proposed to form by similar mechanisms.

The complex and porous microstructure of the inward-growing spinel with alternating bright (A) and dark (B) regions have been observed in previous studies [20,25–27,37] and are suggested to be remnants of the reaction zones. The structure is periodic and the frequency of the alternations can be observed to decrease closer to the alloy interface (compared to the outward/inward oxide interface). The relative amounts of porous region B is difficult to quantify but is similar (30–40%) for all alloys clearly exhibiting the banded structure. The periodic structure is suggested to contain important information on the history of the growth of the secondary corrosion protection and the chemical composition of the alternating regions will be discussed below.

**Chemical composition:** The overall composition of the inward-growing scales show depletion in Fe and a resulting enrichment of all the other alloying elements present in the alloys (Cr, Ni/Al, see Table 3). This is to be expected due to the formation of the outward-growing nearly pure iron oxide and is in good agreement with previous studies [10,20,25]. The diffusivity of Fe in the spinel is orders of magnitudes higher than that of the other cations present in the spinel (see Fig. 10). Thus, as Fe is transported outwards, the inward-growing spinel is enriched in Cr, Al and Ni. Thus, as long as Fe is diffusing outwards, if not efficiently refilled from the alloy, the composition of the inward-growing spinel is time dependent. Thus, the influence of chemical composition of the inward-growing spinel is a complex parameter and, together with the limited spatial resolution of the SEM/EDX analysis, the absolute values should be discussed with caution before the robustness of the system is confirmed.

Nevertheless, by comparing the overall composition detected in the inward-growing spinels (see Table 3) in a more qualitative manner, the amount of Cr, Al and Ni in the spinel increases as the alloy composition of each respective alloying element is increased, as expected. Even though the composition in the inward-growing spinel is observed to change, the influence of alloying elements is not obvious, which can be observed, e.g. on the FeCr alloys, forming spinel oxides with different amounts of Cr but exhibiting similar growth rates (see Fig. 6). However, by comparing the oxide scale thicknesses and chemical composition of the inward-growing scale formed on, e.g. the FeCr(Al) alloys, it can be seen that the slow-growing oxides in the secondary regime (Fe18Cr3Al, Fe25Cr3Al), do all exhibit inward-growing scales with high Cr-contents, whereas the growth rate of the non-protective, thicker oxide scales appear to be more independent of composition of the inward-growing



scales. For the FeCrNi alloys the amount of Cr in the spinel remains relatively high (~35–45%, see Table 3) for all alloys, while an enrichment of Ni in the spinel is observed on the thinner (i.e. slow-growing) oxide scales see, e.g. (Fe18Cr10Ni, Fe18Cr20Ni). Thus, it is suggested that the chemical composition of the inward-growing spinel is an important parameter for attaining a secondary corrosion protection both for FeCrAl alloys and stainless steels.

The structure of the spinel oxide ( $M^{2+}M^{3+}M^{3+}O_4$ ) [52] limits the maximum amount of di- and trivalent ions. While Fe commonly exist as either  $Fe^{2+}$  or  $Fe^{3+}$  the oxidation state of Cr, Al and Ni are more restricted to be  $Cr^{3+}$ ,  $Al^{3+}$  and  $Ni^{2+}$  respectively [52]. Thus, the different alloying elements present do not directly compete for all sites in the spinel oxide. Assuming the above mentioned oxidation states, the  $Cr^{3+}$ ,  $Al^{3+}$  and  $Fe^{3+}$  all compete for the trivalent sites (max 67.7 at%) while  $Ni^{2+}$  and  $Fe^{2+}$  compete for the divalent (max 33.3 at%). The maximum amounts of Cr, Al and Ni observed in the inward-growing spinel in this study are below the maximum amount of trivalent ( $Cr + Al \leq 67.7$  at%) and divalent ( $Ni \leq 33.3$  at%) ions for all the analyzed alloys, except for the higher Ni containing alloy (Fe18Cr20Ni) exhibiting higher amounts of Ni, in the inward-growing oxide after 48 h of exposure (see Table 3). The composition, analyzed by SEM/EDX, is an average composition of a relatively large volume (~1  $\mu m$ ). Thus, the higher amounts of Ni in the inward-growing oxide may be the result of a mixture of, e.g. Ni-rich spinel and NiO. Further investigations of the inward-growing oxides are ongoing, using chemical analysis with higher spatial resolution (STEM/EDX).

Regarding the alternating microstructure of the inward-growing scale (region A and B), the porous structure and small scale of the alternating regions observed makes it difficult to quantify by SEM/EDX. However, the composition is observed to alternate between region A and B (see Table 3). The porous regions (region B) are enriched in Cr compared to the dense region A for all alloys where the regions can be clearly separated. The enrichment of Cr is suggested to be caused by a higher iron depletion from this region, even though the amounts of Al remain almost constant throughout the spinel. The variation in composition between region A and B result in a concentration gradient that changes periodically throughout the spinel. Thus, it is proposed that the banded structure may originate from, or be the reason for, a periodic flux variation caused by the gradient in composition as indicated in this study. The complexity of the microstructure and changing chemical composition of the inward-growing spinel requires a thorough microstructural investigation with higher spatial resolution. Further studies are ongoing to better understand how this microstructure influences the growth rate and protective properties in the secondary corrosion regime.

## 5. Conclusions

This study introduces the concepts of primary and secondary corrosion regimes of Fe-based alloys before and after breakaway as a mean to increase the awareness of the possibilities to improve the protective properties of the oxide scale formed after breakaway.

The oxide scale microstructures in the secondary regime are found to be generic for a wide set of alloy compositions (see Fig. 5) and the results suggest that faster oxide grain boundary diffusion does not alone determine the growth rate in the secondary corrosion regime at 600 °C. Thus, corrosion after breakaway could be modeled similarly for many Fe-based alloys using simplified and generalized modeling tools.

Furthermore, the results show that the oxide growth rate in the secondary corrosion regime may be greatly influenced by the variation in alloy composition for some alloys, e.g. by adding Ni or a combination of Al/Cr, while it has little influence on others. This behavior is shown not to be directly connected to how well the primary corrosion protection withstands the exposure environment (i.e. the incubation time to breakaway). Thus, this indicates that research on the secondary corrosion protection, exhibited by certain alloys, has a large potential to

improve the selection and development of alloys for use in corrosive environments where breakaway corrosion cannot be prevented.

## Conflict of interest

None declared.

## Declaration of Competing Interest

The authors report no declarations of interest.

## Acknowledgements

This work was carried out within the High Temperature Corrosion Centre (HTC) at Chalmers University of Technology and with support from VINNOVA, Sweden's Innovation Agency, within the Metallic Materials programme, that are hereby gratefully acknowledged together with the Swedish Energy Agency and the member companies (AB Sandvik Materials Technology, Kanthal AB, Energiforsk AB, MH Engineering AB, Thermo-Calc Software AB, Valmet Technologies Oy, Sumitomo SHI FW Energia Oy, Babcock and Wilcox Volund A/S and MEC BioHeat and Power A/S). The research was performed in part at the Chalmers Materials Analysis Laboratory, CMAL, and also acknowledges W. Fung, F. Karlsson, J. Phother, M. A. Olivas Ogaz, E. Sechaud at Chalmers university of technology for helping out with exposures and analysis of the primary corrosion protection as well as H. Larsson at KTH royal institute of technology for performing equilibrium calculations on the expected substrate phases.

## Appendix A. Supplementary data

Supplementary data associated with this article can be found, in the online version, at <https://doi.org/10.1016/j.corsci.2020.108961>.

## References

- [1] P. Kofstad, High Temperature corrosion, Elsevier Applied Science, London/New York, 1988.
- [2] N. Birks, G.H. Meier, F.S. Pettit, Introduction to the High-Temperature Oxidation of Metals, Cambridge University Press, 2006.
- [3] D.J. Young, High Temperature Oxidation and Corrosion of Metals, 2nd ed., Elsevier, 2016.
- [4] J. Andersson, T. Helander, L. Höglund, P. Shi, B. Sundman, Thermo-Calc and DICTRA, computational tools for materials science, Calphad 26 (2002) 273–312.
- [5] G.C. Wood, D.P. Whittle, The mechanism of breakthrough of protective chromium oxide scales on Fe-Cr alloys, Corros. Sci. 7 (11) (1967).
- [6] M.G. Hobby, The role of nickel in the high-temperature oxidation of Fe-Cr-Ni alloys in oxygen, Oxid. Metals 1 (1) (1969) 23–54.
- [7] H. Asteman, J. Svensson, M. Norell, L. Johansson, Influence of water vapor and flow rate on the high-temperature oxidation of 304L; effect of chromium oxide hydroxide evaporation, Oxid. Metals 54 (1–2) (2000) 11–26.
- [8] H. Asteman, K. Segerdahl, J.E. Svensson, L.G. Johansson, The influence of water vapor on the corrosion of chromia-forming steels, Mater. Sci. Forum 369–372 (1) (2001) 277–286.
- [9] R. Peraldi, B.A. Pint, Effect of Cr and Ni contents on the oxidation behavior of ferritic and austenitic model alloys in air with water vapor, Oxid. Metals 61 (5–6) (2004) 463–483.
- [10] J. Ehlers, D.J. Young, E.J. Smaardijk, A.K. Tyagi, H.J. Penkalla, L. Singheiser, W. J. Quadakkers, Enhanced oxidation of the 9%Cr steel P91 in water vapour containing environments, Corros. Sci. 48 (11) (2006) 3428–3454.
- [11] J. Pettersson, H. Asteman, J.E. Svensson, L.G. Johansson, KCl induced corrosion of a 304-type austenitic stainless steel at 600 degrees C: the role of potassium, Oxid. Metals 64 (1–2) (2005) 23–41.
- [12] F. Liu, J.E. Tang, T. Jonsson, S. Canovic, K. Segerdahl, J.E. Svensson, M. Halvarsson, Microstructural investigation of protective and non-protective oxides on 11% chromium steel, Oxid. Metals 66 (5–6) (2006) 295–319.
- [13] T. Jonsson, F. Liu, S. Canovic, H. Asteman, J.-E. Svensson, L.-G. Johansson, M. Halvarsson, Influence of  $H_2O(g)$  on the oxide microstructure of the stainless steel 353MA at 900 °C in oxygen, J. Electrochem. Soc. 154 (11) (2007) C603.
- [14] E. Essuman, G.H. Meier, J. Zurek, M. Hänsel, L. Singheiser, W.J. Quadakkers, Enhanced internal oxidation as trigger for breakaway oxidation of Fe-Cr alloys in gases containing water vapor, Scr. Mater. 57 (9) (2007) 845–848.
- [15] C. Pettersson, L.G. Johansson, J.E. Svensson, The influence of small amounts of KCl (s) on the initial stages of the corrosion of alloy Sanicro 28 at 600 degrees C, Oxid. Metals 70 (5–6) (2008) 241–256.

- [16] T. Jonsson, J. Froitzheim, J. Pettersson, J.E. Svensson, L.G. Johansson, M. Halvarsson, The influence of KCl on the corrosion of an Austenitic stainless steel (304L) in oxidizing humid conditions at 600 °C: a microstructural study, *Oxid. Metals* 72 (3–4) (2009) 213–239.
- [17] N.K. Othman, J. Zhang, D.J. Young, Water vapour effects on Fe–Cr alloy oxidation, *Oxid. Metals* 73 (1–2) (2010) 337–352.
- [18] A.N. Hansson, K. Pantleon, F.B. Grumsen, M.A. Somers, Microstructure evolution during steam oxidation of a Nb stabilized austenitic stainless steel, *Oxid. Metals* 73 (1–2) (2010) 289–309.
- [19] J. Pettersson, N. Folkeson, L.-G. Johansson, J.-E. Svensson, The effects of KCl, K<sub>2</sub>SO<sub>4</sub> and K<sub>2</sub>CO<sub>3</sub> on the high temperature corrosion of a 304-type austenitic stainless steel, *Oxid. Metals* 76 (2011) 93–109.
- [20] B. Pujilaksono, T. Jonsson, H. Heidari, M. Halvarsson, J.E. Svensson, L. G. Johansson, Oxidation of binary FeCr alloys (Fe-2.25Cr, Fe-10Cr, Fe-18Cr and Fe-25Cr) in O<sub>2</sub> and in O<sub>2</sub> + H<sub>2</sub>O environment at 600 °C, *Oxid. Metals* 75 (3–4) (2011) 183–207.
- [21] T. Gheno, D. Monceau, D.J. Young, Mechanism of breakaway oxidation of Fe–Cr and Fe–Cr–Ni alloys in dry and wet carbon dioxide, *Corros. Sci.* 64 (2012) 222–233.
- [22] N. Mu, K.Y. Jung, N.M. Yanar, G.H. Meier, F.S. Pettit, G.R. Holcomb, Water vapor effects on the oxidation behavior of Fe–Cr and Ni–Cr alloys in atmospheres relevant to oxy-fuel combustion, *Oxid. Metals* 78 (3–4) (2012) 221–237.
- [23] L. Liu, Z.-G. Yang, M. Zhang, K. Kawamura, T. Maryama, Effect of water vapour on the oxidation of Fe-13Cr-5Ni martensitic alloy at 973 K, *Corros. Sci.* 60 (2012) 90–97.
- [24] J. Lehmusto, B.-J. Skrifvars, P. Yrjas, M. Hupa, Comparison of potassium chloride and potassium carbonate with respect to their tendency to cause high temperature corrosion of stainless 304L steel, *Fuel Process. Technol.* 105 (2013) 98–105.
- [25] T. Jonsson, B. Pujilaksono, H. Heidari, F. Liu, J.-E. Svensson, M. Halvarsson, L.-G. Johansson, Oxidation of Fe-10Cr in O<sub>2</sub> and in O<sub>2</sub>+H<sub>2</sub>O environment at 600 °C: a microstructural investigation, *Corros. Sci.* 75 (2013) 326–336.
- [26] A. Col, V. Parry, C. Pascal, Oxidation of a Fe-18Cr-8Ni austenitic stainless steel at 850 °C in O<sub>2</sub>: Microstructure evolution during breakaway oxidation, *Corros. Sci.* 114 (2017) 17–27.
- [27] T. Jonsson, H. Larsson, S. Karlsson, H. Hooshyar, M. Sattari, J. Liske, J.E. Svensson, L.G. Johansson, High-temperature oxidation of FeCr(Ni) alloys: the behaviour after breakaway, *Oxid. Metals* 87 (3–4) (2017) 333–341.
- [28] S.R.J. Saunders, M. Monteiro, F. Rizzo, The oxidation behaviour of metals and alloys at high temperatures in atmospheres containing water vapour: a review, *Prog. Mater. Sci.* 53 (2008) 775–837.
- [29] A. Fry, S. Osgerby, M. Wright, *Oxydation of Alloys in Steam Environments – A Review*, NPL Report MATC(A)90, 2002.
- [30] M. Montgomery, A. Karlsson, O.H. Larsen, Field test corrosion experiments in Denmark with biomass fuels. Part 1: straw-firing, *Mater. Corros.* 53 (2) (2002) 121–131.
- [31] F.J. Frandsen, Utilizing biomass and waste for power production – a decade of contributing to the understanding, interpretation and analysis of deposits and corrosion products, *Fuel* 84 (10) (2005) 1277–1294.
- [32] P. Henderson, P. Szakalos, R. Pettersson, C. Andersson, J. Hogberg, Reducing superheater corrosion in wood-fired boilers, *Mater. Corros.* 57 (2) (2006) 128–134.
- [33] L. Paz, T. Jonsson, J. Liske, Testing of new materials to combat superheater corrosion in a waste fired CFB boiler, in: 23rd International Conference on Fluidized Bed Conversion, Seoul, South Korea, 2018.
- [34] S.C. Okoro, M. Montgomery, F.J. Frandsen, K. Pantleon, Influence of preoxidation on high-temperature corrosion of a FeCrAl alloy under conditions relevant to biomass firing, *Oxid. Metals* 89 (1–2) (2018) 99–122.
- [35] J. Eklund, M.D. Paz, B. Jönsson, J. Liske, J.E. Svensson, T. Jonsson, Field exposure of FeCrAl model alloys in a waste-fired boiler at 600 °C: the influence of Cr and Si on the corrosion behaviour, *Mater. Corros.* 70 (8) (2019) 1476–1485.
- [36] J. Eklund, B. Jönsson, A. Persdotter, J. Liske, J. Svensson, T. Jonsson, The influence of silicon on the corrosion properties of FeCrAl model alloys in oxidizing environments at 600 °C, *Corros. Sci.* 144 (2018) 266–276.
- [37] T. Jonsson, S. Karlsson, H. Hooshyar, M. Sattari, J. Liske, J.-E. Svensson, L.-G. Johansson, Oxidation after breakdown of the chromium-rich scale on stainless steels at high temperature: internal oxidation, *Oxid. Metals* 85 (2016) 509–536.
- [38] T. Gheno, D. Monceau, D.J. Young, Kinetics of breakaway oxidation of Fe–Cr and Fe–Cr–Ni alloys in dry and wet carbon dioxide, *Corros. Sci.* 77 (2013) 246–256.
- [39] H. Larsson, T. Jonsson, R. Naraghi, Y. Gong, R.C. Reed, J. Ågren, Oxidation of iron at 600 °C – experiments and simulations, *Mater. Corros.* 68 (2) (2017) 133–142.
- [40] S. Bigdeli, L. Kjellqvist, R. Naraghi, L. Höglund, H. Larsson, T. Jonsson, Strategies for High-Temperature Corrosion Simulations of Fe-Based Alloys Using Calphad Approach – Part I, Unpublished, 2020.
- [41] R.F.A. Pettersson, J. Enecker, L. Liu, Role of nickel in the oxidation of Fe–Cr–Ni alloys in air-water vapour atmospheres, *Mater. High Temp.* 22 (3–4) (2005) 269–281.
- [42] R.F.A. Pettersson, Effects of composition on the corrosion of Fe–Ni–Cr alloys in chlorinating and sulfidising environments, *Mater. High Temp.* 26 (3) (2009) 217–222.
- [43] R.Y. Chen, W.Y.D. Yuen, Review of the high-temperature oxidation of iron and carbon steels in air or oxygen, *Oxid. Metals* 59 (1) (2003) 433–468.
- [44] W.W. Smeltzer, Diffusional growth of multiphase scales and subscales on binary alloys: a review, *Mater. Sci. Eng.* 87 (C) (1987) 35–43.
- [45] J. Topfer, S. Aggarwal, R. Dieckmann, Point defects and cation tracer diffusion in (Cr<sub>x</sub>Fe<sub>1-x</sub>)<sub>3-6</sub>O<sub>4</sub> spinels, *Solid State Ionics* 81 (2738) (1995) 251–266.
- [46] J.A.V. Orman, K.L. Crispin, Diffusion in oxides, *Rev. Mineral. Geochem.* 72 (2010) 757–825.
- [47] N. Bertrand, C. Desgranges, D. Poquillon, M.C. Lafont, D. Monceau, Iron oxidation at low temperature (260–500 °C), Air and the Effect of Water Vapor (2010) 139–162.
- [48] G.B. Gibbs, R. Hales, The influence of metal lattice vacancies on the oxidation of high temperature materials, *Corros. Sci.* 17 (1977) 487–507.
- [49] L. Martinelli, F. Balbaud-Célérier, A. Terlain, S. Bosonnet, G. Picard, G. Santarini, Oxidation mechanism of an Fe-9Cr-1Mo steel by liquid Pb–Bi eutectic alloy at 470 °C (Part II), *Corros. Sci.* 50 (9) (2008) 2537–2548.
- [50] I. Kaur, W. Gust, *Fundamentals of Grain and Interface Boundary Diffusion*, Ziegler Press, Stuttgart, 1989.
- [51] T. Jonsson, B. Pujilaksono, A. Fuchs, J.-E. Svensson, L.G. Johansson, M. Halvarsson, The influence of H<sub>2</sub>O on iron oxidation at 600 °C: a microstructural study, *High Temperature Corrosion and Protection of Materials* 7, Ser. Materials Science Forum, 595 (2008) 1005–1012.
- [52] W. Bragg, The structure of the spinel group of crystals, *London Edinburgh Dublin Philos. Mag. J. Sci.* 30 (176) (1915) 305–315.
- [53] R. Dieckmann, M.R. Hilton, T.O. Mason, Defects and cation diffusion in magnetite (VIII): migration enthalpies for iron and impurity cations, *Berichte der Bunsengesellschaft/Phys. Chem. Chem. Phys.* 91 (1) (1987) 59–66.